Hindawi
International Journal of Aerospace Engineering
Volume 2022, Article ID 4048490, 9 pages
https://doi.org/10.1155/2022/4048490

Research Article

Separation Control for a Transonic Convex Corner Flow Using Ramp-Type Vortex Generators

Kao-Chun Su,[1] Kung-Ming Chung ,[2] and Sergey Isaev[3]

[1]Department of Aeronautics and Astronautics, National Cheng Kung University, 1 University Road, East District, Tainan 701, Taiwan
[2]Aerospace Science and Technology Research Center, National Cheng Kung University, 2500 Section 1, Chung-Cheng South Road, Guiren District, Tainan 711, Taiwan
[3]St. Petersburg State University of Civil Aviation, 38 Pilotov Street, St. Petersburg 196210, Russia

Correspondence should be addressed to Kung-Ming Chung; kmchung@mail.ncku.edu.tw

Received 10 August 2022; Revised 19 September 2022; Accepted 14 October 2022; Published 22 October 2022

Academic Editor: Teng Wu

A flap can be used to control wing camber and as a high-lift device. A convex corner is a simplified model of the upper surface of a flap. At transonic speeds, shock-induced boundary layer separation (SIBLS) occurs at greater freestream Mach numbers and deflection angles. This results in energy losses and a reduction in aerodynamic performance. This study installs ramp-type vortex generators (VGs) upstream of a convex corner, and the effect of the height of the VG on SIBLS is determined. As the height of the VG increases, the magnitude of the mean surface pressure upstream of the corner increases and downstream expansion decreases, which results in a reduction in lift. A reduction in peak surface pressure fluctuations, the separation length, and the frequency of shock oscillation is also determined. For flow control and lift enhancement, micro-VGs are more effective.

1. Introduction

Flaps are located at the trailing edges of a fixed wing to control the wing camber and are used to increase lift during takeoff and landing. In the cruise, variable-geometry wing camber control has benefits for transport aircraft that uses deflected flaps [1]. However, the effect of compressibility must be considered. Chung [2] used a convex corner model to simulate the upper surface of a deflected flap. There is significant expansion near the corner's apex and downstream compression. As the freestream Mach number, M, and the deflection angle, η, increase, there is a transition from subsonic to transonic flow and SIBLS occurs. A similarity parameter, β ($M^2\eta/\sqrt{1-M^2}$), is used to characterize a compressible convex corner flow (peak Mach number, M_p, peak pressure fluctuations, and shock oscillation) [3]. If $\beta > 13$, SIBLS occurs and induces low-frequency, high-amplitude shock oscillations [4].

Flow separation reduces the aerodynamic efficiency. Passive or active device has been used to control separated flow [5–8]. A VG is a passive device [9]. An array of VGs is normally attached to a surface at an angle of incidence, α, to introduce streamwise vorticity into the flow near the surface, and the boundary layer is energized to resist adverse pressure gradients and SIBLS. The ratio of the height of a VG, h, to the incoming boundary layer thickness, δ, ($h^* = h/\delta$) is a dominant parameter. Increasing h^* generates stronger vortices [10]. Lee et al. [11] showed that VGs for which $h^* \geqq 1$ prevent SIBLS, but the device drag increases. Micro-VGs ($h^* \leqq 0.5$) incur a smaller drag penalty [12–14].

Ramp-type VGs are robust structurally and are eminently suited to applications in high-speed flows [15–18]. A ramp-type VG forms a counter-rotating vortex pair and is advected by the mean flow. Energetic air is transferred from the primary vortex pair, and the velocity close to the surface depends on the liftoff of the vortices [19]. The gap between ramp-type VGs creates secondary counter-rotating vortices and reduces the interaction between counter-rotating vortex pairs [20]. For an oblique shock reflection with microramp VGs, the momentum flux that is added to the separation bubble increases linearly with h^*. VGs stabilize the interaction (a reduction in shock unsteadiness) more effectively as h^* increases. A distance of 5.7 δ is required for full boundary layer mixing [21].

A deflected flap controls wing camber for an increase in lift, and a convex corner models its upper surface. In the transonic flow regime, SIBLS and peak pressure fluctuations occur for $\beta > 13$ [2]. Shock wave control technologies are required. This study uses ramp-type VGs positioned upstream of a convex corner ($\eta = 13^\circ$ and 15°) for $M = 0.83$ and 0.89 to minimize the adversarial effects of SIBLS. The value of h^* is 0.2, 0.5, 1.0, and 1.5. The mean and fluctuating pressure distributions in the streamwise direction are determined. The locations for flow separation and reattachment with and without the presence of VGs are visualized using oil flow visualization. The effect of VGs on SIBLS and shock oscillation is determined. Before discussing the results, details of the experiment setup are outlined next.

2. Experimental Technique

2.1. Transonic Wind Tunnel. The experiments were conducted in a blowdown transonic wind tunnel at the Aerospace Science and Technology Research Center of the National Cheng Kung University. The facility comprises two compressors, two air dryers (dew point in normal operation ≈ -40°C), a cooling water system, three storage tanks (total volume = 180 m^3), and a tunnel. The constant area test section is 600 mm × 600 mm and is 1500 mm in length. The test section was assembled using perforated top/bottom walls with 6% porosity (to alleviate reflected shock and expansion waves) and solid side walls (to reduce background noise). The stagnation pressure, p_0, is 172 ± 0.5 kPa, and the stagnation temperature is 28°C–32°C. M is 0.83 and 0.89 ± 0.01. This determines the respective unit Reynolds numbers: 2.33 and 2.41 × 10^7/m.

2.2. Test Models. The test model comprised a flat plate and an instrumentation plate with/without an array of ramp-type VGs, as shown in Figure 1. The flat plate is 450 mm long and 150 mm wide. The interchangeable instrumentation plate is 170 mm in length and 150 mm in width. A convex corner with η of 13° and 15° is located at 500 mm from the leading edge of the flat plate. The value of δ at 25 mm upstream of the convex corner is approximately 7 mm [2], and the respective Reynolds numbers based on δ are 1.63 and 1.69 × 10^5 for $M = 0.83$ and 0.89. The test without the presence of VGs is the baseline case.

Lin [12] showed that a VG is effective at least 20 h upstream of the location of flow separation. This study uses an array of ramp-type VGs that are positioned 3 mm upstream of the convex corner. Seventeen pressure taps are machined perpendicular to the surface of the test model along the centerline: 5 pressure taps ahead of the VG and 12 pressure taps downstream of the convex corner. The spacing between the pressure taps is 6 mm. The configuration of the VGs is shown in Figure 2, and the parameters of the VGs are shown in Table 1. The length, l, is 1 δ, and the width, w, is 0.5 δ. The spacing, D, between the VGs is 3 δ. This gives an array with seven VGs [22]. The value of α is 15° [23].

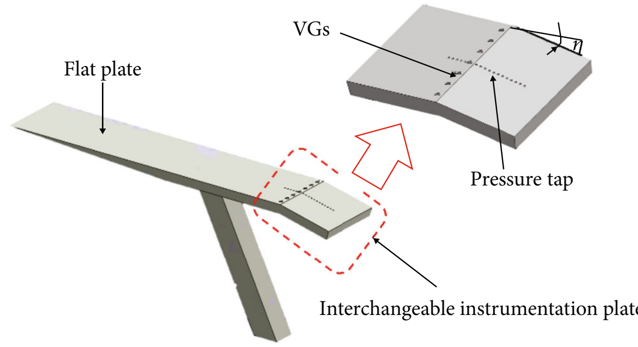

Figure 1: A sketch of the test configuration.

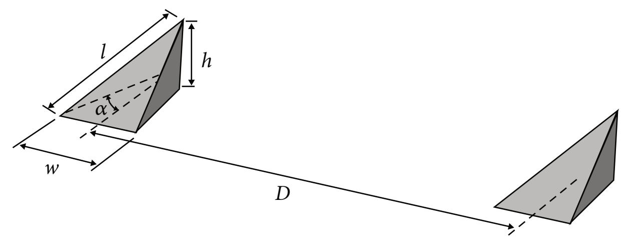

Figure 2: A sketch of the ramp-type VGs.

Table 1: Geometrical parameters for ramp-type VGs.

Parameter	Value
h^*	0.2, 0.5, 1.0, and 1.5
l/δ	1.0
D/δ	3.0
w/δ	0.5
α	15°

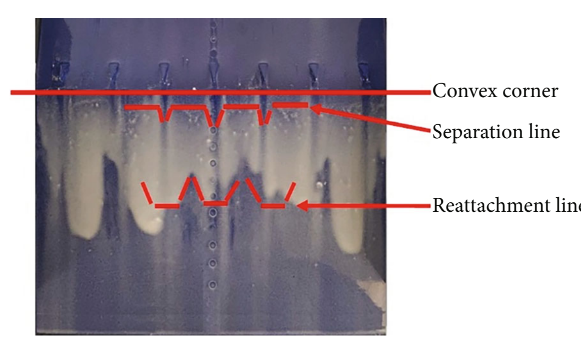

Figure 3: An example of oil flow visualization for $h^* = 0.5$.

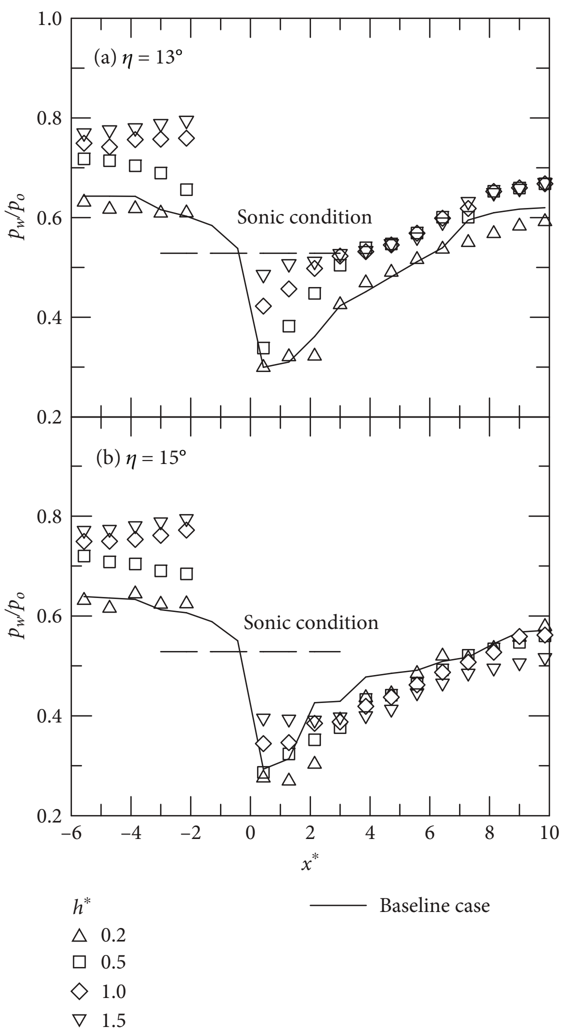

FIGURE 4: Mean surface pressure distribution for $M = 0.83$.

2.3. Instrumentation and Data Acquisition System. Kulite pressure transducers (XCS-093-25A, B screen) with a natural frequency of 200 kHz were used to measure the mean and fluctuating surface pressures. The nominal outer diameter of the Kulite sensors is 2.36 mm, and the diameter of the pressure-sensitive element is 0.97 mm. External amplifiers (Ectron Model E713) with a roll-off frequency of approximately 140 kHz were used to improve the signal-to-noise ratio. A National Instrument (CI SCXI) was used to trigger all input channels and to record data. Ten Kulite sensors were installed in the streamwise direction on a flat plate. The experimental uncertainty for the mean surface pressure coefficient, p_w/p_0, and the surface fluctuating pressure coefficient, σ_p/p_w, is determined. Using 10 Kulite sensors, the standard deviation for p_w/p_0 is 1.24% and the mean value for σ_p/p_w is 0.97%.

Oil flow visualization technique is used to determine the points at which separation and reattachment occur and the separation length, L. A compound mixture of titanium dioxide, oil, and oleic acid was applied to the surface of the instrumentation plate. An accumulation of titanium dioxide signifies the separation location. The end of the deflected streak line denotes the flow reattachment which exhibits a corrugated pattern if there are VGs, as shown in Figure 3. The mean positions for separation and reattachment are calculated.

3. Results and Discussion

3.1. Mean Surface Pressure Distribution. The distribution of p_w/p_0 for $M = 0.83$ is shown in Figure 4. For the baseline case, there is a near incipient separation for $\eta = 13°$ and shock oscillation for $\eta = 15°$ [24]. The horizontal axis is the normalized streamwise location, x^* (x/δ), and the origin is the corner's apex. There is no data for $x^* = -2$ to 0 because this is the position of the VGs. The sonic condition ($p_w/p_0 = 0.5283$) is also shown for reference. For the baseline case, the p_w/p_0 distribution exhibits slight upstream expansion, significant expansion near the corner's apex, and downstream compression. For VGs for which $h^* = 0.2$ and $\eta = 13°$, the VGs have little effect on the p_w/p_0 distribution. The minimum p_w/p_0, $(p_w/p_0)_{\min}$, is located farther

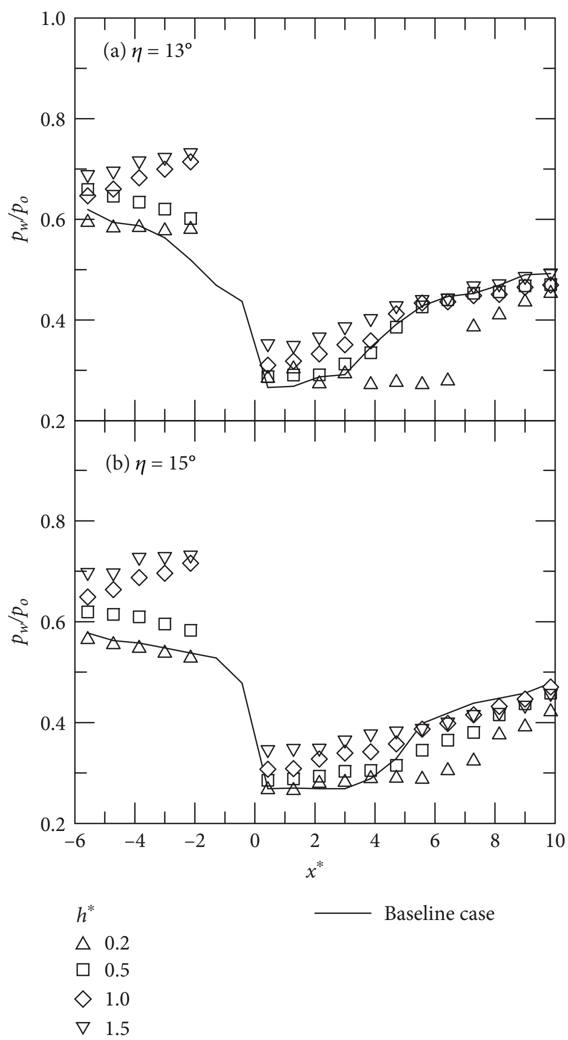

Figure 5: Mean surface pressure distribution for $M = 0.89$.

downstream than that for the baseline case because the VGs induce expansion waves [25]. An increase in h^* affects the p_w/p_0 distribution. For VGs for which $h^* = 0.5 - 1.5$, there is an increase in the value of p_w/p_0 upstream of the corner as h^* increases. This shows an increase in device drag, particularly for $h^* = 1.0$ and 1.5. An increase in the value of $(p_w/p_0)_{\min}$ downstream of the corner represents less expansion or a decrease in the value of M_p as h^* increases. The p_w/p_0 distribution for $\eta = 15°$ is similar to that for $\eta = 13\circ$. For the baseline case, there is a distinctive kink at $x^* \approx 2$ which indicates SIBLS [2]. If there are VGs, the kink moves downstream. This represents a delay in flow separation.

The p_w/p_0 distribution for $M = 0.89$ is shown in Figure 5. For the baseline case, compression occurs farther downstream than that for $M = 0.83$. Bouhadji and Braza [26] showed that a hyperbolic character for a high subsonic flow results in a sweep for a perturbation action propagating downstream. This causes greater convection for $M = 0.89$. For $\eta = 13°$ and 15°, the compression for $h^* = 0.2$ occurs farther downstream, so there is a greater convection effect, but not for $h^* \geqq 0.5$. h^* has a similar effect on the p_w/p_0 distribution as that for $M = 0.83$.

For the baseline case, Figure 6 shows the effect of β on $(p_w/p_0)_{\min}$ and M_p. The value of $(p_w/p_0)_{\min}$ (0.267-0.303) decreases (or M_p increases) as β increases. For VGs for which $h^* = 0.2$ and 0.5, the value of $(p_w/p_0)_{\min}$ (0.266-0.299) and M_p shows a minor deviation from the baseline case. An increase in the value of h^* results in an increase in $(p_w/p_0)_{\min}$ and a decrease in M_p. For VGs for which $h^* = 1.0$ and 1.5, there is less flow expansion near the convex corner, $(p_w/p_0)_{\min} = 0.308 - 0.486$, so the lift force is reduced if a deflected control surface is used for a fixed wing.

3.2. Surface Pressure Fluctuations. The σ_p/p_w distribution for $M = 0.83$ is shown in Figure 7. For the baseline case, there is a minor variation in the value of σ_p/p_w upstream and downstream of the corner, but not near the corner's apex. The respective peak values for σ_p/p_w, $(\sigma_p/p_w)_{\max}$ for $\eta = 13°$ and 15°, are 6.9% and 6.2% at $x^* = 2.14$. VGs reduce the amplitude of $(\sigma_p/p_w)_{\max}$. For $h^* = 0.2$, there is a reduction in the values of $(\sigma_p/p_w)_{\max}$ to 1.6% and 1.0% for $\eta = 13°$ and 15°. An increase in h^* results in a more decrease in $(\sigma_p/p_w)_{\max}$. For $\eta = 15°$

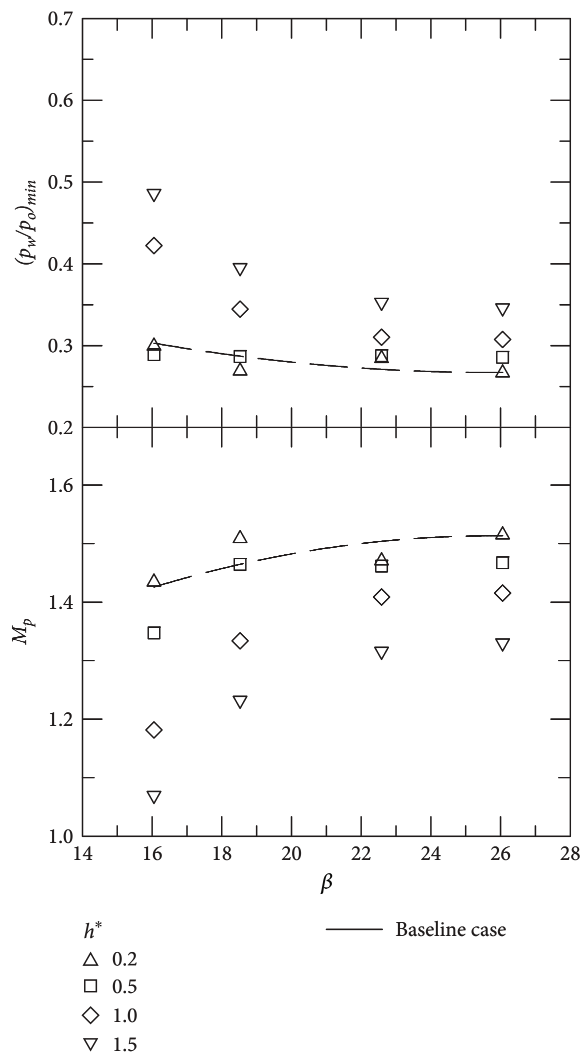

FIGURE 6: The effect of VGs on flow expansion near the corner's apex.

(more extensive separated flow), VGs have less effect on $(\sigma_p/p_w)_{\max}$ than that for $\eta = 13^\circ$ (near incipient separation), so the effectiveness of VGs depends on the status of the separated flow (incipient separation or strong shock oscillation).

The σ_p/p_w distribution for $M = 0.89$ is shown in Figure 8. The respective values of $(\sigma_p/p_w)_{\max}$ are 8.6% and 10.3% at $x^* = 3.86$ for $\eta = 13^\circ$ and 15°. For VGs for which $h^* = 0.2$, there is a reduction in the value of $(\sigma_p/p_w)_{\max}$ at $x^* = 9.00$ for $\eta = 13^\circ$ and $x^* = 7.28$ for $\eta = 15^\circ$. The location x^* of $(\sigma_p/p_w)_{\max}$ for $M = 0.89$ is larger than that for $M = 0.83$ is due to a hyperbolic character for a high subsonic flow [26]. This is consistent with the downstream pressure recovery process for a convex corner flow, as shown in Figure 5. An increase in h^* results in a decrease in $(\sigma_p/p_w)_{\max}$, particularly for $\eta = 13^\circ$.

The relationship between the value of $(\sigma_p/p_w)_{\max}$ (6.2%-10.3%) and β for the baseline case is shown in Figure 9. The presence of VGs results in a decrease in the value of $(\sigma_p/p_w)_{\max}$ (4.6%-10.2%), particularly as h^* increases because stronger induced vortices affect shock oscillation.

3.3. Shock Oscillation. SIBLS results in intense pressure fluctuations [27–30]. Dolling and Brusniak [31] studied the intermittent pressure signals to determine the unsteadiness of shock motion (shock oscillation). A conditional analysis technique (two-threshold method, THM) was used to determine the shock zero-crossing frequency, f_s. The upper and lower thresholds are $p_w + 3\sigma_p$ and $p_w + 6\sigma_p$. The time between consecutive passages of shock over a pressure sensor is determined. The pressure signal is then converted into a boxcar of amplitude unity, as shown in Figure 10.

Figure 11 shows the relationship between f_s and M_p. For the baseline case, the value of f_s ranges from 1320 Hz to 640 Hz. There is a decrease as M_p increases. Variation in f_s is related to the length of a separation bubble [4]. The presence of VGs reduces the shock oscillation where $f_s = 929$ Hz-126 Hz.

For SIBLS, the unsteady shock motion is related to successive contractions and expansions of a separation bubble. The normalized separation length, L^* (L/δ), can be used as a length scale to characterize shock unsteadiness [4]. The variation of L^* with M_p is shown in Figure 12. The value

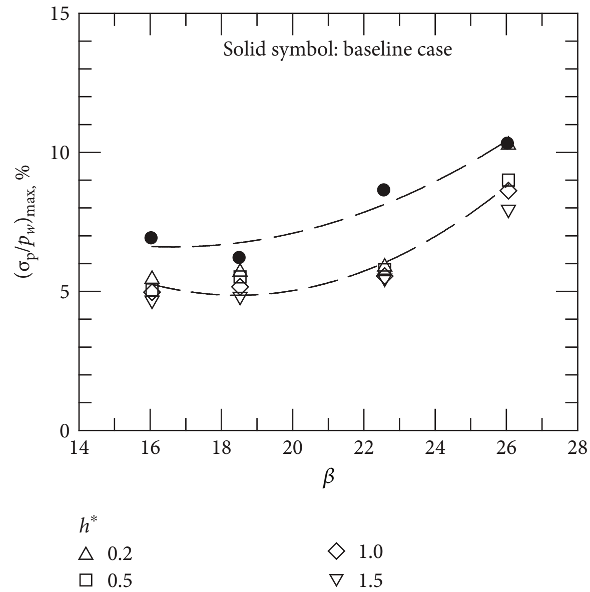

Figure 7: Distribution of surface pressure fluctuations for $M = 0.83$.

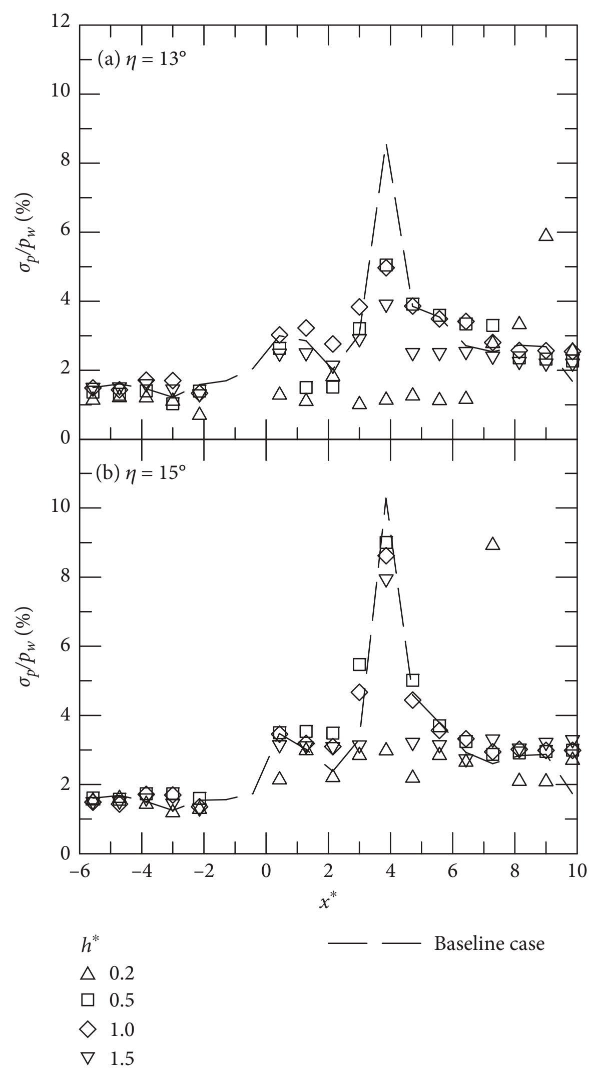

Figure 8: Distribution of surface pressure fluctuations for $M = 0.89$.

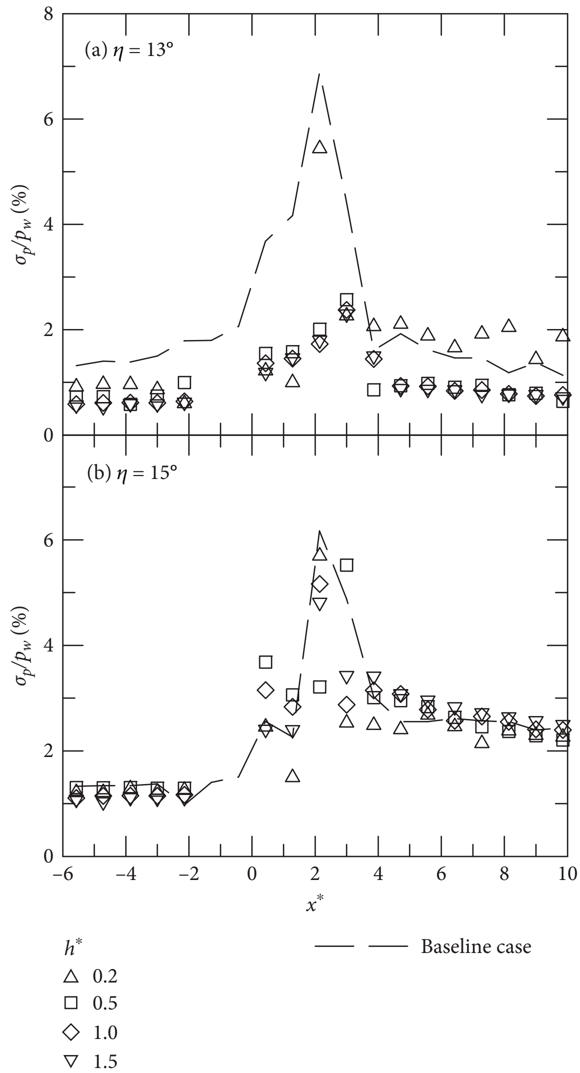

Figure 9: The effect of h^* on peak pressure fluctuations.

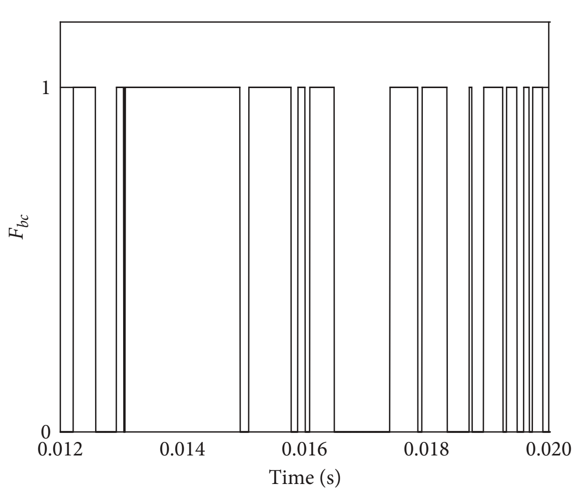

Figure 10: Boxcar in the THM.

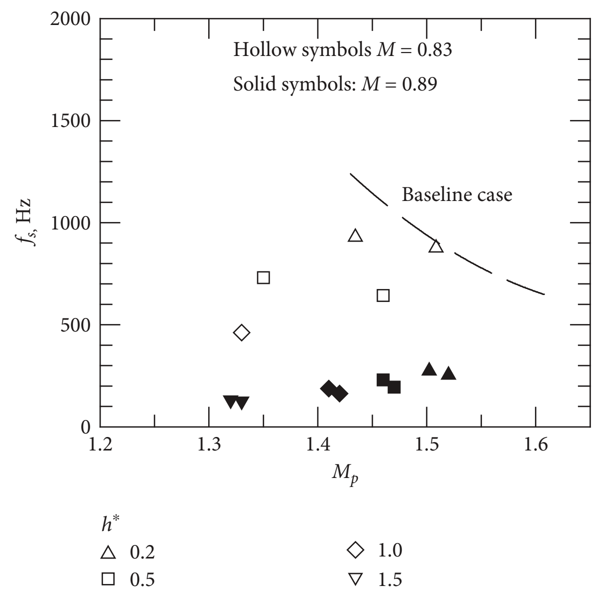

Figure 11: Shock zero-crossing frequency.

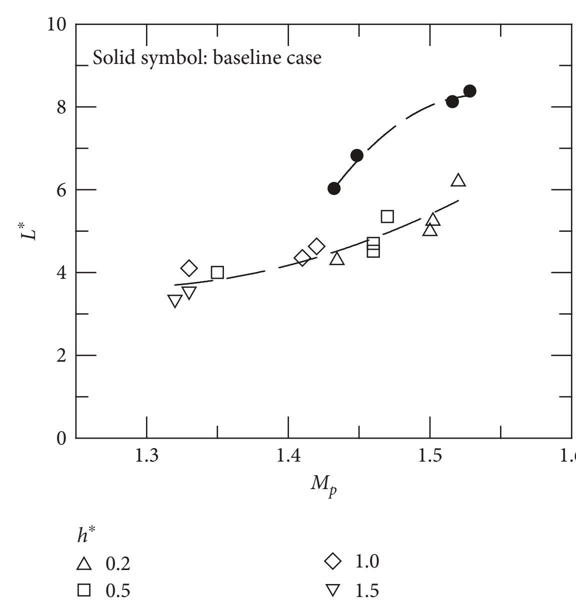

Figure 12: Normalized separation length versus peak Mach number.

of L^* (6.00-8.35) increases as M_p increases. The presence of VGs results in a decrease in the value of L^* (3.35-6.19). The decrease is more significant as h^* increases. This result agrees with the results of Verma and Manisankar [32].

The variation in the Strouhal number, St ($f_s L/U_p$), with M_p is shown in Figure 13, where U_p is the peak velocity. For the baseline case, the value of St ranges from 0.09 to 0.12. When the VGs are positioned upstream of the convex corner, there is a decrease in the value of M_p, L^*, and St. For $M = 0.89$, the value of St (0.007-0.02) decreases as h^* increases because there are stronger induced vortices.

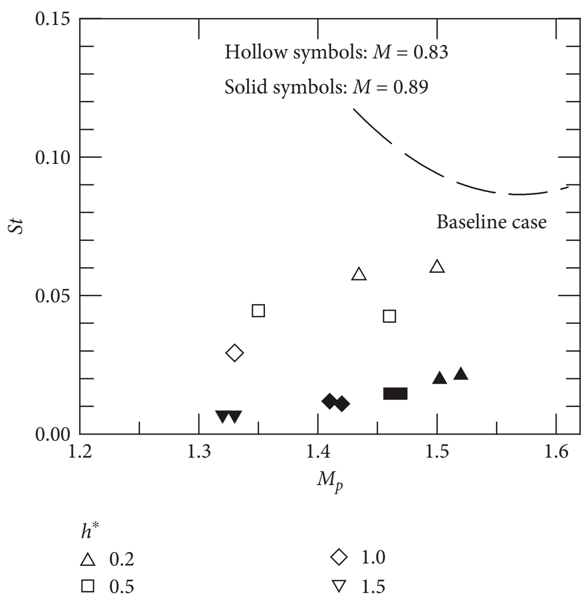

FIGURE 13: St versus peak Mach number.

4. Conclusions

This study determines the effect of the height of ramp-type VGs on a transonic convex corner flow. VGs for which $h^* = 0.2$ have a minor effect on the p_w/p_0 distribution. The presence of VGs induces streamwise vorticity that propagates downstream. This results in an extension in the low-pressure region and a slower downstream pressure recovery process, particularly for $M = 0.89$. An increase in h^* (1.0 and 1.5) results in a mean surface pressure upstream of the convex corner that is greater in magnitude and less expansion near the corner. This indicates that there is greater device drag and a reduction in the effectiveness of the VGs. The values for $(\sigma_p/p_w)_{\max}$ (4.6%-10.2%) and L^* (3.35-6.19) decrease as h^* increases because the presence of VGs prevents SIBLS. The analysis in terms of f_s (929 Hz-126 Hz) and St (0.007-0.059) shows less shock oscillation, particularly for VGs for which $h^* \leqq 0.5$.

Nomenclature

D: Spacing between vortex generators
f_s: Shock zero-crossing frequency, Hz
h: Height of vortex generator
h^*: Normalized height of vortex generator, h/δ
L: Mean separation length
L^*: Normalized mean separation length, L/δ
l: Length of vortex generator
M: Freestream Mach number
M_p: Peak Mach number
p_0: Stagnation pressure
p_w: Local mean surface pressure
$(P_w/p_0)_{\min}$: The minimum pressure coefficient
SIBLS: Shock-induced boundary layer separation
St: Strouhal number, $f_s L/U_p$
THM: Two-threshold method
x: Coordinate along the centerline of model surface
x^*: Normalized streamwise distance, x/δ
U_p: Peak velocity
VG: Vortex generator
w: Width of vortex generator
α: Angle of incidence of vortex generator
β: Similarity parameter, $M^2\eta/\sqrt{1-M^2}$
δ: Incoming boundary-layer thickness
η: Convex corner angle, degree
σ_p: Standard deviation of surface pressure
σ_p/p_w: Fluctuating pressure coefficient
$(\sigma_p/p_w)_{\max}$: Peak fluctuating pressure coefficient.

Data Availability

Data is available upon request.

Conflicts of Interest

The authors declare that they have no conflicts of interest.

Acknowledgments

The authors acknowledge the financial support from the Ministry of Science and Technology, Taiwan (MOST 110-2923-E-006-006-MY3).

References

[1] A. Bolonkin and G. B. Gilyard, *Estimated Benefits of Variable-Geometry Wing Camber Control for Transport Aircraft*, NASA TM-1999-206586, 1999.

[2] K. M. Chung, "Investigation on transonic convex-corner flows," *Journal of Aircraft*, vol. 39, no. 6, pp. 1014–1018, 2002.

[3] K. M. Chung, P. H. Chang, and K. C. Chang, "Flow similarity in compressible convex-corner flows," *AIAA Journal*, vol. 50, no. 4, pp. 985–988, 2012.

[4] K. M. Chung, K. H. Lee, and P. H. Chang, "Low-frequency shock motion in transonic convex-corner flows," *AIAA Journal*, vol. 55, no. 6, pp. 2109–2112, 2017.

[5] A. N. Shahrbabaki, M. Bazazzadeh, and R. Khoshkhoo, "Investigation on supersonic flow control using nanosecond dielectric barrier discharge plasma actuators," *International Journal of Aerospace Engineering*, vol. 2021, Article ID 2047162, 14 pages, 2021.

[6] Y. Z. Wang, H. D. Zhang, Y. Wu, Y. H. Li, and Y. F. Zhu, "Compressor airfoil separation control using nanosecond plasma actuation at low Reynolds number," *AIAA Journal*, vol. 60, no. 2, pp. 1171–1185, 2022.

[7] P. Y. Yang, X. Zhang, and T. R. Yue, "A comparative study on post-stall flow separation control mechanism of steady and unsteady plasma actuators," *Physics of Fluids*, vol. 34, no. 5, article 057105, 2022.

[8] J. Q. Liu, R. Q. Chen, Q. C. Song, Y. C. You, and Z. Y. Shi, "Active flow control of helicopter rotor based on cross flow jet," *International Journal of Aerospace Engineering*, vol. 2021, Article ID 9299470, 19 pages, 2021.

[9] I. Maghsoudi, M. A. Vaziry, and M. Mahmoodi, “Experimental investigation of flow and distortion mitigation by mechanical vortex generators in a coupled serpentine inlet-turbofan engine system,” *Chinese Journal of Aeronautics*, vol. 33, no. 5, pp. 1375–1391, 2020.

[10] Y. Ichikawa, S. Koike, Y. Ito et al., “Size effects of vane-type rectangular vortex generators installed on high-lift swept-back wing flap on lift force and flow fields,” *Experiments in Fluids*, vol. 62, no. 8, p. 160, 2021.

[11] S. Lee, E. Loth, and H. Babinsky, “Normal shock boundary layer control with various vortex generator geometries,” *Computers and Fluids*, vol. 49, no. 1, pp. 233–246, 2011.

[12] J. C. Lin, “Review of research on low-profile vortex generators to control boundary-layer separation,” *Progress in Aerospace Sciences*, vol. 3, no. 4-5, pp. 389–420, 2002.

[13] N. K. Singh, “Control of laminar separation bubble using vortex generators,” *Journal of Applied Fluid Mechanics*, vol. 12, no. 3, pp. 891–905, 2019.

[14] X. K. Li, K. Yang, and X. D. Wang, “Experimental and numerical analysis of the effect of vortex generator height on vortex characteristics and airfoil aerodynamic performance,” *Energies*, vol. 12, no. 5, p. 959, 2019.

[15] S. Lee, E. Loth, N. J. Georgiadis, and J. R. DeBonis, “Effect of Mach number on flow past microramps,” *AIAA Journal*, vol. 49, no. 1, pp. 97–110, 2011.

[16] S. Lee and E. Loth, “Impact of ramped vanes on normal shock boundary-layer interaction,” *AIAA Journal*, vol. 50, no. 10, pp. 2069–2079, 2012.

[17] A. G. Panaras and F. K. Lu, “Micro-vortex generators for shock wave/boundary layer interactions,” *Progress in Aerospace Sciences*, vol. 74, pp. 16–47, 2015.

[18] D. Sun, J. Chen, L. C. Chen, P. Liu, Q. Guo, and X. Yuan, “On the wake structure of a micro-ramp vortex generator in hypersonic flow,” *Physics of Fluids*, vol. 32, no. 12, article 126111, 2020.

[19] J. P. S. Sandhu, S. Ghosh, S. Subramanian, and P. Sharma, “Evaluation of ramp-type micro vortex generators using swirl center tracking,” *AIAA Journal*, vol. 56, no. 9, pp. 3449–3459, 2018.

[20] R. R. Martis and A. Misra, “Separation attenuation in swept shock wave–boundary-layer interactions using different microvortex generator geometries,” *Shock Waves*, vol. 27, no. 5, pp. 747–760, 2017.

[21] R. H. M. Giepman, F. F. J. Schrijer, and B. W. van Oudheusden, “Flow control of an oblique shock wave reflection with micro-ramp vortex generators: effects of location and size,” *Physics of Fluids*, vol. 26, no. 6, article 066101, 2014.

[22] K. M. Chung, K. C. Su, and K. C. Chang, “Micro-vortex generators on transonic convex-corner flow,” *Aerospace*, vol. 8, no. 9, p. 268, 2021.

[23] S. Wang and S. Ghaemi, “Effect of vane sweep angle on vortex generator wake,” *Experiments in Fluids*, vol. 60, no. 1, p. 24, 2019.

[24] K. M. Chung, “Unsteadiness of transonic convex-corner flows,” *Experiments in Fluids*, vol. 37, no. 6, pp. 917–922, 2004.

[25] H. A. Holden and H. Babinsky, *Vortex Generators Near Shock/Boundary Layer Interactions*, AIAA Paper, 2004.

[26] A. Bouhadji and M. Braza, “Organised modes and shock-vortex interaction in unsteady viscous transonic flows around an aerofoil: part I: Mach number effect,” *Computers & Fluids*, vol. 32, no. 9, pp. 1233–1260, 2003.

[27] J. P. Piponnian, J. F. Dussauge, and P. Dupont, “A simple model for low-frequency unsteadiness in shock-induced separation,” *Journal of Fluid Mechanics*, vol. 629, pp. 87–108, 2009.

[28] E. Touber and N. D. Sandham, “Low-order stochastic modelling of low-frequency motions in reflected shock-wave/boundary-layer interactions,” *Journal of Fluid Mechanics*, vol. 671, pp. 417–465, 2011.

[29] L. J. Mears, A. Baldwin, M. Y. Ali, R. Kumar, and F. S. Alvi, “Spatially resolved mean and unsteady surface pressure in swept SBLI using PSP,” *Experiments in Fluids*, vol. 61, no. 4, p. 92, 2020.

[30] S. G. Guo, Y. Wu, and H. Liang, “Strong interactions of incident shock wave with boundary layer along compression corner,” *Chinese Journal of Aeronautics*, vol. 33, no. 12, pp. 3149–3157, 2020.

[31] D. S. Dolling and L. Brusniak, “Separation shock motion in fin, cylinder, and compression ramp induced turbulent interactions,” *AIAA Journal*, vol. 27, no. 6, pp. 734–742, 1989.

[32] S. B. Verma and C. Manisankar, “Control of a Mach reflection-induced interaction using an array of vane-type vortex generators,” *Shock Waves*, vol. 28, no. 4, pp. 815–828, 2018.